New Physics: Sae Mulli,
Vol. 65, No. 6, June 2015, pp. 542∼549
DOI: 10.3938/NPSM.65.542

Structural, Electrical and Multiferroic Properties of Nb-doped $Bi_7Fe_3Ti_3O_{21}$ Thin Films

Chinnambedu Murugesan RAGHAVAN · Jin Won KIM · Sang Su KIM*
Department of Physics, Changwon National University, Changwon, Changwon 641-773, Korea

(Received 20 March 2015 : revised 25 April 2015 : accepted 10 May 2015)

The effects of donor Nb^{5+}-ion doping on the structural, electrical, and multiferroic properties of an Aurivillius $Bi_7Fe_3Ti_3O_{21}$ thin film were investigated. Incorporation of Nb^{5+}-ions into the Ti^{4+}-sites of the $Bi_7Fe_3Ti_3O_{21}$ thin film resulted in a substantial improvement of its electrical and multiferroic properties. From the study of the electrical properties, the $Bi_7Fe_3Ti_{2.94}Nb_{0.06}O_{21+\delta}$ thin film exhibited a low leakage current density of 5.11×10^{-6} A/cm^2 at 100 kV/cm, which was about one order of magnitude lower than that of the untreated $Bi_7Fe_3Ti_3O_{21}$ thin film. The ferroelectric $P-E$ hysteresis loops of the $Bi_7Fe_3Ti_{2.94}Nb_{0.06}O_{21+\delta}$ thin film showed a large remnant polarization ($2P_r$) of 20.6 μC/cm^2 at 630 kV/cm whereas the $2P_r$ value measured for the untreated $Bi_7Fe_3Ti_3O_{21}$ thin film was 3.5 μC/cm^2 at 318 kV/cm. Furthermore, a well-saturated magnetic hysteresis loop with an enhanced magnetization was observed for the $Bi_7Fe_3Ti_{2.94}Nb_{0.06}O_{21+\delta}$ thin film at room temperature.

PACS numbers: 77.80.-e, 77.80.Fm
Keywords: Nb-doped $Bi_7Fe_3Ti_3O_{21}$ thin film, Chemical solution deposition, Electrical properties, Multiferroic properties

I. INTRODUCTION

Multiferroic materials, *i.e.*, materials with two or more ferroic orders, offer a promising platform for the upcoming generation of computer digital memories. Multiferroics combine the best functionalities of ferroelectric random access memory, namely fast writing, low power consumption, and high endurance, with the nondestructive read operation of magnetic random access memory for use in modern electronic storage devices [1–3]. However, the major drawbacks that continue to hinder the implementation of these materials in practical devices are operational temperature (most of the multiferroics only function well below ambient conditions), a low magnitude of magnetization, and a low ferroelectric polarization [1]. Therefore, it is technologically important to develop novel single-phase multiferroic materials that exhibit both a large ferroelectric polarization and magnetization at room temperature.

Currently, special attention is paid to Aurivillius phase Fe-contained ferroelectric compounds with a bismuth-layered structure (BLSF) with the general formula $Bi_{n+1}Fe_{n-3}Ti_3O_{3n+3}$ (n $\geq$ 4, where n refers to the number of perovskite layers) for effective multiferroic applications [4–10]. These materials were found to simultaneously exhibit ferroelectric and ferromagnetic properties near ambient conditions [5–7]. Furthermore, they showed strong coupling of the electrical and magnetic orders close to room temperature [4, 9]. The crystal structure of these compounds consists of perovskite-like $(Bi_{n-1}Fe_{n-3}Ti_3O_{3n+1})^{2-}$ slabs sandwiched in between fluorite-like bismuth-oxygen $(Bi_2O_2)^{2+}$ layers along the c-axis [11]. The electrical properties of these materials are mainly controlled by the $(Bi_2O_2)^{2+}$ layers; hence, they generally show a high resistivity along the c-axis [12] There are several reports on the structural, electrical, and multiferroic properties of the $Bi_5FeTi_3O_{15}$ (n = 4) and $Bi_6Fe_2Ti_3O_{18}$ (n = 5) Aurivillius compounds [5–7,13–16]. The $Bi_7Fe_3Ti_3O_{21}$ (BFTO21) (n = 6) Aurivillius structure recently gained special interest because of

*E-mail: sskim@changwon.ac.kr

the advantages it holds, such as its nontoxic Pb-free nature, stable phase, room-temperature multiferroic properties, and unprecedented visible light photocatalytic activity for the decomposition of organic pollutants [17,18]. Recently, the coexistence of ferroelectric and magnetic properties was observed for Gd-doped BFTO21 bulk ceramics; however, the reported results showed the ferroelectric hysteresis loops to be leaky with a low polarization and the magnetization-magnetic field hysteresis loops were shown to be unsaturated [18]. The low ferroelectric polarization of the BFTO21 was related to the large leakage current density, which is primarily caused by the oxygen vacancies in the lattice [13]. Moreover, the weak magnetization in the BFTO21 was attributed to the antiferromagnetic spiral spin structure [13,18].

The aim of the present study is to improve the electrical and multiferroic properties of BFTO21 thin films by the doping of donor Nb^{5+}-ions into the Ti^{4+}-sites of the Aurivillius structure. Doping with donor Nb^{5+}-ions is known to be an effective approach for overcoming oxygen vacancies, to reduce the leakage current, and to improve the ferroelectric properties of the BLSF compounds [19–21]. A reported computational study inferred the preference of the Nb^{5+}-ion to enter the Ti-site [19]. The ionic radius of the Nb^{5+}-ion (0.64 Å) is slightly larger than that of the Ti^{4+}-ion (0.60 Å); hence, doping of the Ti-sites of BFTO21 with Nb^{5+}-ions would be expected to introduce distortion. This structural distortion is known to be crucial for the improvement of the multiferroic properties of BLSF compounds [4,13]. To the best of our knowledge the effects of donor Nb^{5+}-ion doping on the structural, electrical, and multiferroic properties of the BFTO21 thin film have not yet been reported. Therefore, in this study, both pure $Bi_7Fe_3Ti_3O_{21}$ and Nb^{5+}-ion doped $Bi_7Fe_3Ti_{2.94}Nb_{0.06}O_{21+\delta}$ (BFTNbO21) thin films were prepared on a $Pt(111)/Ti/SiO_2/Si(100)$ substrate by using a chemical solution method. The effects of doping on the microstructural properties of the thin films were investigated by using X-ray diffraction patterns and Raman spectra. The electrical and multiferroic properties of the thin films were also investigated, and the results are discussed in detail.

II. EXPERIMENTAL DETAILS

The BFTO21 and the BFTNbO21 thin films were prepared on $Pt(111)/Ti/SiO_2/Si(100)$ substrates by using a chemical solution method. The raw materials, bismuth nitrate pentahydrate $[Bi(NO_3)_3{\cdot}5H_2O]$, iron nitrate nonahydrate $[Fe(NO_3)_3{\cdot}9H_2O]$, titanium isopropoxide $[Ti(OCH(CH_3)_2)_4]$, and niobium pentaethoxide $[Nb(OC_2H_5)_5]$ were used for the preparation of the precursor solutions. Ethylene glycol ($OH(CH_2)_2OH$) and 2-methoxyethanol ($CH_3O(CH_2)_2OH$) were mixed at room temperature by constant stirring, and was used as the solvent. To this solvent mixture, acetic acid (CH_3COOH) was added as a catalyst. The measured quantities of bismuth nitrate pentahydrate and iron nitrate nonahydrate were added sequentially to the above solvent containing the catalyst at 30 min intervals. Separately, a homogeneous solution of 2-methoxyethanol and acetylacetone ($CH_3COCH_2COCH_3$), which was used as a stabilizing agent, was prepared at room temperature in a glove box, thereafter titanium isopropoxide and niobium pentaethoxide were dissolved sequentially in this mixture and stirred for 1.5 h. Then, the Ti-Nb solution was added to the Bi-Fe solution to form the BFTNbO21 precursor, and the final mixture was stirred for an additional 2 h. The pure BFTO21 precursor solution was prepared in the same manner for reference purposes. The overall concentrations of both of the precursor solutions were calculated to ensure final concentrations of 0.1 M.

The BFTO21 and the BFTNbO21 precursor solutions were coated on the $Pt(111)/Ti/SiO_2/Si(100)$ substrates by using a spin-coating method at an angular speed of 3000 rpm for 20 s, subsequent to which the wet thin films were exposed to two-stage prebaking processes at 200 °C and 360 °C for 5 min on a hot plate for drying and removing organic impurities, respectively. The coating and prebaking processes were repeated 15 times to obtain the desired film thickness. Finally, both of the thin films were annealed at 600 °C for 3 min by rapid thermal annealing under an oxygen atmosphere for crystallization. Platinum electrodes with areas of 1.54×10^{-4} cm^2 were deposited on the top surfaces of the thin films by ion sputtering through a metal shadow mask to enable the electrical properties to be measured.

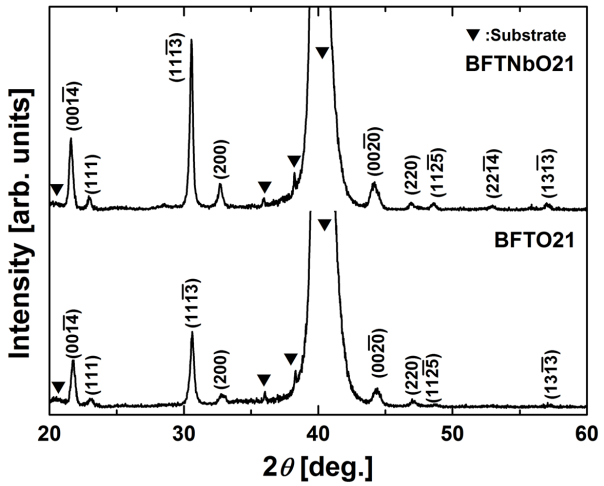

Fig. 1. XRD patterns of the BFTO21 and the BFTNbO21 thin films deposited on Pt(111)/Ti/SiO_2/Si(100) substrates.

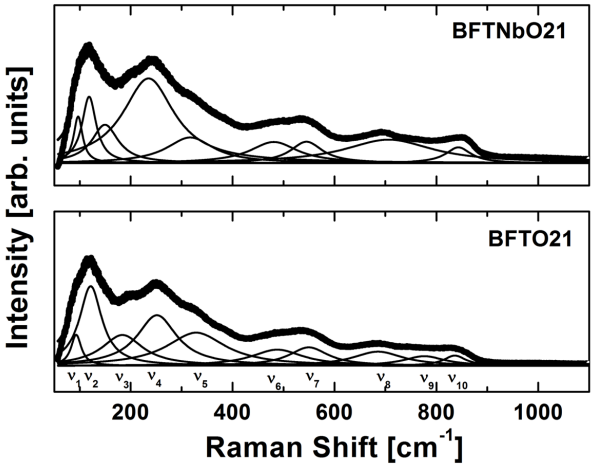

Fig. 2. Raman scattering spectra with their fitted curves (thick solid lines) and their decomposed active modes (thin solid lines) of the BFTO21 and the BFTNbO21 thin films measured at room temperature.

The crystal structures of the BFTO21 and the BFTNbO21 thin films were analyzed by using an X-ray diffractometer (Rigaku, MiniFlex II) and a Raman spectroscope (Jasco, NRS-3100). The leakage current densities and the dielectric properties of the thin films were measured by using an electrometer (Keithley, 6517A) and a low frequency impedance analyzer (HP, 4192A), respectively. The ferroelectric polarization-electric field ($P-E$) hysteresis loops of the thin films were traced at a frequency of 1.25 kHz by using a standardized ferroelectric test system (Radiant Technologies Inc., Precision LC). The room-temperature magnetic properties of the thin films were measured by using a physical property measurement system (Quantum Design Inc., PPMS-7).

III. RESULTS AND DISCUSSION

Figure 1 shows the X-ray diffraction (XRD) patterns of the BFTO21 and the BFTNbO21 thin films. The XRD study revealed the formation of Aurivillius phase orthorhombic structures, which were observed for both thin films without any traces of secondary or impurity phases. The XRD peaks were indexed with respect to an orthorhombic crystal structure with a $F2mm$ space group [8, 18]. Nb-doping did not lead to significant changes in the positions of the XRD peaks, and hence there was no notable change in the lattice parameters, which could be attributed to a low concentration of Nb^{5+}-ion dopant. However, the XRD intensities of the major peaks of BFTNbO21 were significantly stronger compared to those of the BFTO21 thin film. The BFTNbO21 thin film exhibited stronger intensities of the diffraction peaks corresponding to the $(00\overline{1}4)$, $(11\overline{1}3)$, (200), $(00\overline{2}0)$, and (111) planes. Furthermore, the weak diffraction peak corresponding to the $(22\overline{1}4)$ plane, which was detected for the BFTNbO21 thin film, was absent from the BFTO21 thin film. These results indicated the enhanced crystallinity resulting from Nb^{5+}-ion doping of the Ti^{4+}-sites of the Aurivillius BFTO21 thin film.

The specific site occupied by the Nb^{5+}-ion in the BFTO21 and the resulting structural changes were further investigated using Raman spectroscopic studies. Figure 2 shows the Raman scattering spectra of the BFTO21 and the BFTNbO21 thin films measured at room temperature, which were obtained by using a solid-state Nd-YAG laser with a wavelength of 532 nm. The positions of the individual peaks displayed by the thin films were calculated by fitting the measured spectra and decomposing them into their individual Lorentz components as shown in Fig. 2. It is well known that typical BLSF structures exhibit two specified spectral regions, a low frequency region below 200 cm^{-1}, which is related to the vibrations of the Bi^{3+}-ions, and a high frequency region above 200 cm^{-1}, which is ascribed to the stretching

Table 1. Assignments of the Raman active phonon modes for the BFTO21 and the BFTNbO21 thin films.

	Raman frequencies (cm^{-1})									
Thin films	ν_1	ν_2	ν_3	ν_4	ν_5	ν_6	ν_7	ν_8	ν_9	ν_{10}
BFTO21	93	121	183	251	328	487	549	685	776	836
BFTNbO21	97	118	150	236	317	481	545	706	-	843

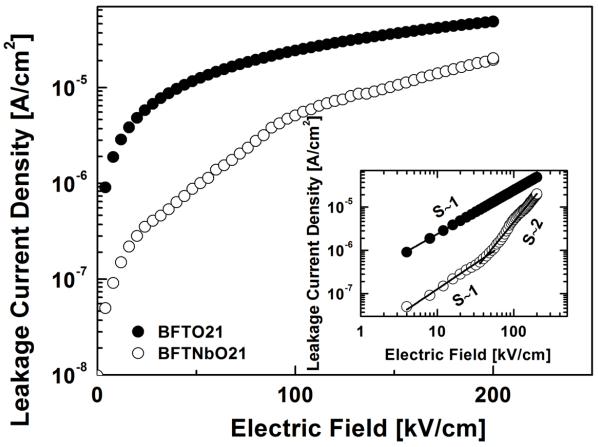

Fig. 3. Leakage current densities of the BFTO21 and the BFTNbO21 thin films and the $\log(J)$-$\log(E)$ characteristics of the thin films.

vibration and torsional bending of the $Ti(Fe)O_6$ octahedra [22,23]. The assigned Raman frequencies for the BFTO21 and the BFTNbO21 thin films are given in Table 1.

As shown in Fig. 2, the ν_1 (93 cm^{-1} (BFTO21) and 97 cm^{-1} (BFTNbO21)), ν_2 (121 cm^{-1} (BFTO21) and 118 cm^{-1} (BFTNbO21)), and ν_3 (183 cm^{-1} (BFTO21) and 150 cm^{-1} (BFTNbO21)) modes are those attributed to the vibrations of the Bi^{3+}-ions [18, 22, 23]. The ν_4 (251 cm^{-1} (BFTO21) and 236 cm^{-1} (BFTNbO21)) and ν_5 (328 cm^{-1} (BFTO21) and 317 cm^{-1} (BFTNbO21)) modes are attributed to the O-Ti-O bending vibrations [24]. Formation of the ν_6 (487 cm^{-1} (BFTO21) and 481 cm^{-1} (BFTNbO21)) and ν_7 (549 cm^{-1} (BFTO21) and 545 cm^{-1} (BFTNbO21)) modes are assigned for the opposing extensions of the external apical oxygen atoms of the octahedra [24]. The origin of the ν_8 (685 cm^{-1} (BFTO21) and 706 cm^{-1} (BFTNbO21)) mode could be attributed to the Bi-Fe-O vibrations of the perovskite block [22]. The ν_9 (776 cm^{-1} (BFTO21)) and the ν_{10} (836 cm^{-1} (BFTO21) and 843 cm^{-1} (BFTNbO21)) modes are attributed to the symmetric stretching modes of the [$Ti(Fe)O_6$] octahedra [23,24].

As seen in Table 1, compared with the BFTO21, the BFTNbO21 showed slight shifts of its phonon modes. As shown in Fig. 2, the ν_9 mode disappeared from the spectrum of the BFTNbO21 thin film. Furthermore, the intensities of the Raman modes in the high frequency region were noticeably stronger for the BFTNbO21 compared to the BFTO21. These changes in the high-frequency Raman modes might be indicative of distortion in the pseudo-perovskite block of the BLSF structure, a possible consequence of the slightly larger ionic radius of the Nb^{5+}-ion compared to that of the Ti^{4+}-ion, which would lead to distortion of the BFTO21 octahedra [18,20,25]. Furthermore, the broadening of the low-frequency Raman bands may also be attributed to the structural effect of doping on the pseudo-perovskite blocks of the BLSF lattice [18]. The results of the Raman spectral study of the BFTO21 and the BFTNbO21thin films were well correlated to the XRD study to confirm the orthorhombic structure.

The trend displayed by the leakage current densities (J) with respect to the applied electric fields (E) for the BFTO21 and the BFTNbO21 thin films are shown in Fig. 3. The plots in Fig. 3 enabled the measured leakage current densities of the BFTO21 and the BFTNbO21 thin films to be determined as 2.43×10^{-5} and 5.11×10^{-6} A/cm^2 at 100 kV/cm, respectively; thus, the leakage current density of the BFTNbO21 thin film was about one order of magnitude lower than that of the BFTO21 thin film. It is widely accepted that the large leakage current density observed for the Fe-contained Aurivillius BLSF structure is mainly due to the presence of oxygen vacancies, poor surface morphology, and the electronic instability of the Fe^{3+}-ion [26]. In addition, the tendency of Bi to evaporate under the conditions under which the thin films are prepared; *i.e.*, the drying and annealing processes, is well known [26, 27]. Thus, the large leakage current observed for the BFTO21 thin film could be attributed to the combined effect of the

Bi-deficiency generated in this way accompanied by the occurrence of oxygen vacancies [27]. The decrease in the leakage current density of the BFTNbO21 thin film could be related to the suggested ability of the donor Nb^{5+}-ions in the Ti^{4+}-sites of the BFTO21 to compensate for the oxygen vacancies [21,28]. The following Kroger-Vink equation can be used to explain this compensation

$$\begin{aligned} Nb_2O_5 \;&\rightarrow\; 2(Nb_{Ti}^{\cdot}) + 5O_O^X + 2e \\ 1/2O_2 + V_O^{\cdot\cdot} + 2e &\leftrightarrow O_o, \end{aligned} \tag{1}$$

where $Nb_{Ti}^{\cdot}, O_O^X, V_O^{\cdot\cdot}$, and e represent an Nb^{5+}-ion with one positive charge for the Ti^{4+}-ion, a null charge on oxygen, an oxygen vacancy with two positive charges, and an electron charge, respectively. From the above equations, it is clear that the electrons donated by the Nb^{5+}-ion compensate for the oxygen vacancies, thereby controlling the leakage current density in the BFTNbO21 thin film [21,29]. Eventually, doping of the Ti^{4+}-sites with donor Nb^{5+}-ions would also be able to facilitate the formation of cationic vacancies at the Bi-sites of the BFTO21 to maintain the charge neutrality [30]. Nevertheless, the mobility of the cationic vacancies is extremely low as compared to the mobility of the oxygen ions. Therefore, the formation of cationic vacancies has less of an impact on the electrical conductivity of the BFTNbO21 thin film [30,31].

The origin of the observed leakage current was probed by investigating the leakage current mechanisms, which was done by plotting log (J) versus log (E) as shown in the inset of Fig. 3. Based on these plots, it has been inferred that the BFTO21 thin film exhibits Ohmic conduction behavior across the whole measurement region with a slope value of S∼1, and hence that the observed conduction properties of the BFTO21 thin film could mainly be attributed to thermally stimulated electrons [32]. The Ohmic conduction mechanism can be expressed as

$$J = e\mu N_e E, \tag{2}$$

where e is the electron charge, μ is the free carrier mobility, N_e is the density of the thermally stimulated electrons, and E is the applied electric field [32]. In contrast to BFTO21, the BFTNbO21 thin film displayed a change of conduction behavior with an increasing applied electric field. As shown in the inset of Fig. 3, the plot of

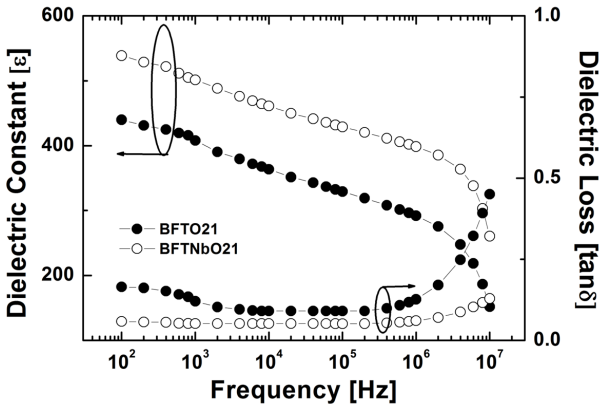

Fig. 4. Frequency-dependent dielectric properties of the BFTO21 and the BFTNbO21 thin films.

the BFTNbO21 thin film has two segments, which were linearly fitted with slope values of S∼1 and S∼2, and are indicative of Ohmic and space charge limited (SCL) conduction mechanisms, respectively. According to the SCL conduction mechanism, the flow of electric current is attributed to the flow of charged free carriers rather than thermally injected electrons [33]. The onset of SCL conduction in the BFTNbO21 thin film was observed to occur at ∼ 50 kV/cm, thereafter the observed conduction was mainly due to the charged carriers. The current density for the SCL conduction can be expressed as

$$J_{SCL} = \left(\frac{9\mu\varepsilon_0\varepsilon_r\theta}{8}\frac{V^2}{d^3}\right) \tag{3}$$

where V is the applied voltage, ε_r is the dielectric constant, ε_0 is the permittivity of free space, d is the thickness of thin film, and θ is the ratio of the total density of free electrons to trapped electrons [32]. Thus, the transport property of the BFTO21 was significantly influenced by the Nb^{5+}-ion insertion into the Ti^{4+}-sites of the Aurivillius structure.

In ferroelectric thin films, oxygen vacancies act as space charge components and contribute to the electrical polarization; thus, the presence of an increasing number of oxygen vacancies leads to high dielectric loss in these thin films [31]. Therefore, it is important to study the dielectric properties of ferroelectric thin films. The variation of the dielectric constant and the dielectric loss values of the BFTO21 and the BFTNbO21 thin films with respect to the applied frequencies were measured at room temperature as shown in Fig. 4. The applied frequencies were varied in the range from 10^2 to 10^7 Hz. From

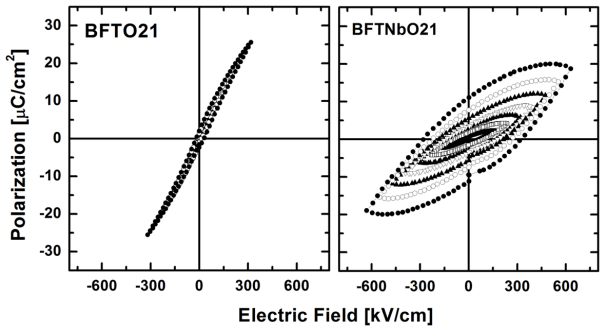

Fig. 5. Ferroelectric polarization-electric field ($P-E$) hysteresis loops of the BFTO21 and the BFTNbO21 thin films.

Fig. 4, the measured dielectric constant (ε) and dielectric loss values of the BFTO21 and the BFTNbO21 thin films were 407 and 0.120 and 501 and 0.052, respectively, at an applied frequency of 1 kHz. The low dielectric loss value of the BFTNbO21 thin film could be attributed to the reduced contribution of space charge components, indicating that doping with pentavalent Nb^{5+}-ions effectively reduces the concentration of oxygen vacancies [31].

The co-existence of the ferroelectric and ferromagnetic properties of the BFTO21 and the BFTNbO21 thin films were investigated at room temperature. The ferroelectric $P-E$ hysteresis loops of the thin films were measured with triangular pulses at a frequency of 1.25 kHz as shown in Fig. 5. The stability of the structure against electrical breakdown was dramatically enhanced when the Ti^{4+}-sites of the BFTO21 thin film were doped with Nb^{5+}-ions. In Fig. 5 it can be seen that the BFTO21 thin film attained electrical breakdown at a low applied electric field of 318 kV/cm, whereas the BFTNbO21 thin film was stable up to 630 kV/cm against electrical breakdown. The measured remnant polarization ($2P_r$) and coercive electric field ($2E_c$) values of the BFTO21 and the BFTNbO21 thin films were 3.5 μC/cm^2 and 47 kV/cm at 318 kV/cm and 20.6 μC/cm^2 and 595 kV/cm at 630 kV/cm, respectively. The ferroelectric polarization that was measured for the BFTNbO21 thin film is larger than that reported for BFTO21 bulk ceramics doped with Gd^{3+}-ions (that is, Gd^{3+}- ions doped into the Bi-site of the BFTO21). This study found a good correlation between the leakage current density and the ferroelectric properties. The low leakage current density of the BFTNbO21 thin film could be related to its enhanced

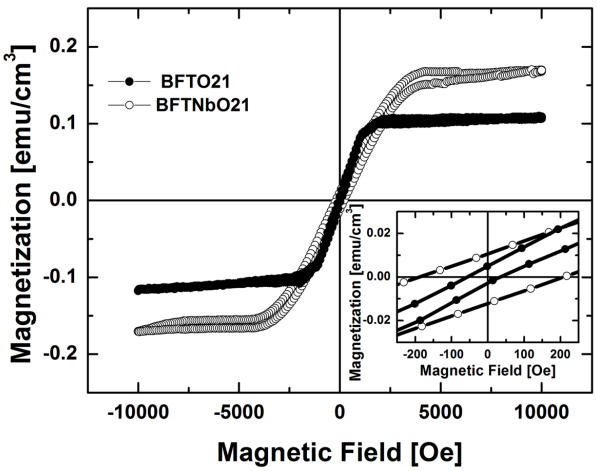

Fig. 6. Magnetization-magnetic field ($M-H$) hysteresis loops of the BFTO21 and the BFTNbO21 thin films measured at room temperature and an inset showing an enlargement of the low-field region of the $M-H$ curves indicating the ferromagnetism.

polarization and good stability against electrical breakdown. It has been well proven that the presence of oxygen vacancies could lead to domain pinning in ferroelectric thin films, a phenomenon responsible for preventing the ferroelectric switching necessary to achieve polarization [27,34]. Doping with donor Nb^{5+}-ions avoids domain pinning by reducing the number of highly mobile oxygen vacancies, which in turn enhances the ferroelectric polarization in the BFTNbO21 thin film [27, 28]. Therefore, the observed large polarization in the BFTNbO21 thin film could be attributed to a considerable reduction of the number of oxygen vacancies resulting from donor Nb^{5+}-ion doping. It has already been noted that the doping of donor Nb^{5+}-ions into the Ti^{4+}-sites of BFTO21 leads to the formation of cationic vacancies to maintain the charge neutrality in the Aurivillius structure; thus, the formed cationic vacancies facilitate domain movement, which in turn favors the large polarization in the BFTNbO21 thin film [35]. Furthermore, the octahedral distortion induced by inserting the Nb^{5+}-ions, with their comparatively larger ionic radii, into the Ti^{4+}-sites, could influence the multiferroic properties of the BFTNbO21 thin film.

The magnetization (M) versus magnetic field (H) plots of the BFTO21 and the BFTNbO21 thin films measured at room temperature are shown in Fig. 6. As seen in the figure, both of the thin films showed well-saturated ferromagnetic hysteresis loops. Doping of the

Ti^{4+}-sites of BFTO21 with Nb^{5+}-ions enhanced both the magnetization and the coercive magnetic field values of the BFTNbO21 thin film, which can clearly be observed on the enlarged $M-H$ plot as shown in the inset of Fig. 6. The plot enabled the determination of the measured remnant magnetization ($2M_r$) and coercive magnetic field ($2H_c$) values of the BFTO21 and the BFTNbO21 thin films as 0.0089 emu/cm^3 and 0.11 kOe and 0.023 emu/cm^3 and 3.95 kOe, respectively, at an applied magnetic field of 10 kOe. Srinivas *et al.* [8] and Sun *et al.* [18] reported dominant antiferromagnetic behavior for BFTO21 bulk ceramics. In contrast, in this study, the weak ferromagnetic properties observed for the BFTO21 thin film might be attributed to the overlapping of the trapped electrons in the oxygen vacancies with the adjacent *d*-orbitals of the neighboring Fe^{3+}-ions in the Aurivillius structure [36]. The magnetic hysteresis loop of the BFTO21 thin film was well saturated compared with those reported for the BFTO21 and the Gd-doped BFTO21 bulk ceramics [8,18]. The increase in the $2M_r$ value of the BFTNbO21 thin film might be attributed to the structural distortion induced by Nb^{5+}-ion doping of the Ti^{4+}-site of BFTO21 [13, 18]. Furthermore, the breakdown of the balance in the antiparallel sub-lattice magnetization of the Fe^{3+}-ions as a result of Nb^{5+}-ion doping could also be considered responsible for the increased magnetization observed for the BFTNbO21 thin film [37]. In overall consideration, Nb^{5+}-ion doping plays a significant role in the improvement of the electrical, dielectric, and multiferroic properties of the Aurivillius BFTO21 thin film.

IV. CONCLUSIONS

In summary, Aurivillius BFTO21 and BFTNbO21 thin films were deposited on Pt(111)/Ti/SiO_2/Si(100) substrates by using a chemical solution deposition method. Both of the thin films crystallized in Aurivillius phase orthorhombic structures without any trace of secondary or impurity phases, as was confirmed by means of X-ray diffraction and Raman spectroscopic studies. The electrical and multiferroic properties were influenced to a remarkable extent by the presence of donor Nb^{5+}-ions with which the BFTO21 lattice was doped. This doping resulted in a low leakage current density, low dielectric loss, large ferroelectric polarization, and large magnetization for the BFTNbO21 thin film. Defect chemistry, which includes compensation for oxygen vacancies, the stabilization of the Aurivillius structure, and structural distortion induced by the donor Nb^{5+}-ions could explain the enhanced electrical and multiferroic properties of the BFTNbO21 thin film. The observed results suggest that the BFTNbO21 thin film would be suitable for use as a storage element in memory devices, and this investigation opens a window for the elemental doping and structural engineering of Aurivillius compounds.

ACKNOWLEDGEMENTS

This research is financially supported by Changwon National University in 2015∼2016.

REFERENCES

[1] J. F. Scott, NPG Asia Mater. **5**, 1 (2013).
[2] R. Ramesh and N. A. Spaldin, Nat. Mater. **6**, 21 (2007).
[3] S. -W. Cheong and M. Mostovoy, Nat. Mater. **6**, 13 (2007).
[4] L. Keeney, T. Maity, M. Schmidt, A. Amann and N. Deepak *et al.*, J. Am. Ceram. Soc. **96**, 2339 (2013).
[5] H. Sun, X. Lu, T. Xu, J. Su and Y. Jin *et al.*, J. Appl. Phys. **111**, 124116 (2012).
[6] Z. Liu, J. Yang, X. W. Tang, L. H. Yin and X. B. Zhu *et al.*, Appl. Phys. Lett. **101**, 122402 (2012).
[7] X. Y. Mao, W. Wang and X. B. Chen, Solid State Commun. **147**, 186 (2008).
[8] A. Srinivas, M. M. Kumar, S. V. Suryanarayana and T. Bhimasankaram, Mater. Res. Bull. **34**, 989 (1999).
[9] A. Srinivas, D. -W. Kim, K. S. Hong and S. V. Suryanarayana, Mater. Res. Bull. **39**, 55 (2004).
[10] S. Patri, R. Choudhary and B. Samantaray, J. Electroceram. **20**, 119 (2008).
[11] N. A. Lomanova, M. I. Morozov, V. L. Ugolkov and V. V. Gusarov, Inorg. Mater. **42**, 189 (2006).
[12] X. Mao, W. Wang, X. Chen and Y. Lu, Appl. Phys. Lett. **95**, 082901 (2009).

[13] F. Z. Huang, X. M. Lu, T. T. Xu, Y. Y. Liu and W. N. Su *et al.*, Thin Solid Films **520**, 6489 (2012).

[14] C. M. Raghavan, J. W. Kim, J. Y. Choi, J. -W. Kim and S. S. Kim, Ceram. Int. **41**, 3277 (2015).

[15] J. -B. Li, Y. P. Huang, G. H. Rao, G. Y. Liu and J. Luo *et al.*, Appl. Phys. Lett. **96**, 222903 (2010).

[16] W. Bai, Y. Q. Gao, J. Y. Zhu, X. J. Meng and T. Lin *et al.*, J. Appl. Phys. **109**, 064901 (2011).

[17] X. Li, Z. Ju, F. Li, Y. Huang and Y. Xie *et al.*, J. Mater. Chem. A **2**, 13366 (2014).

[18] S. Sun, G. Wang, Y. Huang, J. Wang and R. Peng *et al.*, RSC Adv. **4**, 30440 (2014).

[19] H. Hao, H. -X. Liu, X. -M. Min and S. -X. Ouyang, Int. J. Quantum Chem. **111**, 669 (2011).

[20] J. -H. Park, J. -S. Bae, B. -E. Jun, B. -C. Choi and J. -H. Jeong, Appl. Phys. A **86**, 63 (2007).

[21] S. Shulman, D. Damjanovic and N. Setter, J. Am. Ceram. Soc. **83**, 528 (2000).

[22] S. Kojima, R. Imaizumi, S. Hamazaki and M. Takashige, Jpn. J. Appl. Phys. **33**, 5559 (1994).

[23] S. -T. Zhang, Y. -F. Chen, Z. -G. Liu and N. -B. Ming, J. Appl. Phys. **97**, 104106 (2005).

[24] C. Shao, Y. Lu, D. Wang and Y. Li, J. Eur. Ceram. Soc. **32**, 3781 (2012).

[25] A. Yokoi and H. Ogawa, Mater. Sci. Eng. B **129**, 80 (2006).

[26] W. Wang, J. Sun, X. Mao and X. Chen, J. Phys. D: Appl. Phys. **41**, 155418 (2008).

[27] H. Sun, J. Zhu, H. Fang and X. Chen, J. Appl. Phys. **100**, 074102 (2006).

[28] A. Z. Simoes, E. C. Aguiar, A. Ries, E. Longo and J. A. Varela, Mater. Lett. **61**, 588 (2007).

[29] J. Hou, R. V. Kumar, Y. Qu and D. Krsmanovica, Scr. Mater. **61**, 664 (2009).

[30] T. Mihara, H. Yoshimori, H. Watanabe and C. A.P.de Araujo, Jpn. J. Appl. Phys. **34**, 5233 (1995).

[31] I. Coondoo, A. K. Jha and S. K. Agarwal, J. Eur. Ceram. Soc. **27**, 253 (2007).

[32] C. Wang, M. Takahashi, H. Fujino, X. Zhao and E. Kume *et al.*, J. Appl. Phys. **99**, 054104 (2006).

[33] J. Wu, J. Wang, D. Xiao and J. Zhu, AIP Adv. **1**, 022138 (2011).

[34] Y. Noguchi and M. Miyayama, Appl. Phys. Lett. **78**, 1903 (2001).

[35] I. Coondoo, A. K. Jha and S. K. Agarwal, Ceram. Int. **33**, 41 (2007).

[36] H. Sun, X. Lu, J. Su, T. Xu and C. Ju *et al.*, J. Phys. D: Appl. Phys. **45**, 385001 (2012).

[37] W. -S. Kim, Y. -K. Jun, K. H. Kim and S. -H. Hong, J. Magn. Magn. Mater. **321**, 3262 (2009).